The Astrophysical Journal Letters, 905:L26 (8pp), 2020 December 20 https://doi.org/10.3847/2041-8213/abcda9

The Optical Luminosity–Time Correlation for More than 100 Gamma-Ray Burst Afterglows

M. G. Dainotti[1,2,3,4], S. Livermore[5], D. A. Kann[6], L. Li[7], S. Oates[8], S. Yi[9], B. Zhang[10], B. Gendre[11], B. Cenko[12,13], and N. Fraija[14]

[1] Interdisciplinary Theoretical & Mathematical Science Program, RIKEN (iTHEMS), 2-1 Hirosawa, Wako, Saitama, 351-0198, Japan; mdainotti@stanford.edu
[2] Space Science Institute, Boulder, CO, USA
[3] Astronomical Observatory, Jagiellonian University, ul. Orla 171, 31-501 Kraków, Poland; dainotti@oa.uj.edu.pl
[4] SLAC National Accelerator Laboratory, 2575 Sand Hill Road, Menlo Park, CA 94025, USA; dainotti@slac.stanford.edu
[5] Department of Physics and Astronomy, Tufts University, 419 Boston Avenue, Medford, MA 02155 USA; samantha.livermore@tufts.edu
[6] Instituto de Astrofísica de Andalucía (IAA-CSIC), Glorieta de la Astronomía s/n, E-18008 Granada, Spain
[7] ICRANet, Piazza della Repubblica 10, I-65122 Pescara, Italy; liang.li@icranet.org
[8] School of Physics and Astronomy, University of Birmingham, Birmingham B15 2TT, UK
[9] School of Physics and Physical Engineering, Shandong Provincial Key Laboratory of Laser Polarization and Information Technology, Qufu Normal University, Qufu 273165, People's Republic of China
[10] Department of Physics and Astronomy, University of Nevada, Las Vegas, NV 89154, USA
[11] OzGrav University of Western Australia, Crawley, WA 6009, Australia
[12] Astrophysics Science Division, NASA Goddard Space Flight Center, MC 661, Greenbelt, MD 20771, USA
[13] Joint Space-Science Institute, University of Maryland, College Park, MD 20742, USA
[14] Instituto de Astronomia, Universidad Nacional Autonoma de Mexico, Circuito Exterior, C.U., A. Postal 70-264, 04510 Mexico D.F., Mexico
Received 2020 October 29; revised 2020 November 25; accepted 2020 November 25; published 2020 December 21

Abstract

Gamma-ray bursts (GRBs) are fascinating events due to their panchromatic nature. Their afterglow emission is observed from sub-TeV energies to radio wavelengths. We investigate GRBs that present an optical plateau, leveraging on the resemblance with the X-ray plateau shown in many GRB light curves (LCs). We comprehensively analyze all published GRBs with known redshifts and optical plateau observed mostly by the Neil Gehrels Swift Observatory (Swift). We fit 267 optical LCs and show the existence of the plateau in 102 cases, which is the largest compilation so far of optical plateaus. For 56 Swift GRBs with optical and X-ray plateaus, we compare the rest-frame end time at both wavelengths ($T^*_{\rm opt}$, $T^*_{\rm X}$), and conclude that the plateau is achromatic between $T^*_{\rm opt}$ and $T^*_{\rm X}$. We also confirm the existence of the two-dimensional relations between $T^*_{\rm opt}$ and the optical luminosity at the end of the plateau emission, which resembles the same luminosity–time correlation in X-rays (Dainotti et al. 2013). The existence of this optical correlation has been demonstrated for the largest sample of optical plateaus in the literature to date. The squared scatter in this optical correlation is smallest for the subset of the Gold GRBs with a decrease in the scatter equivalent to 52.4% when compared to the scatter of the entire GRB sample.

Unified Astronomy Thesaurus concepts: Gamma-ray bursts (629)

1. Introduction

Gamma-ray bursts (GRBs) are the most luminous objects in the universe, with their luminosities spanning over 8 orders of magnitude. Due to their brightness, we can observe GRBs up to high redshift (Tanvir et al. 2009). Thus, GRBs can be good candidates for use as standard candles because they would extend the Hubble diagram beyond Type Ia supernovae (SNe Ia), observed up to $z < 2.3$ (Riess et al. 2018). To use GRBs as standard candles, we need to better understand their emission mechanisms. GRBs are traditionally classified as short (SGRBs) and long (LGRBs), depending on the prompt emission duration: $T_{90} \leqslant 2$ s or $T_{90} \geqslant 2$ s, respectively[15] (Mazets et al. 1981; Kouveliotou et al. 1993). LGRBs may originate from the collapse of massive stars (the Collapsar model; Woosley 1993), while SGRBs could originate from the merger of two neutron stars (NSs) or an NS and a black hole (BH) (Abbott et al. 2017). To distinguish between these different models, we must classify GRBs according to their phenomenology. The GRB prompt emission is observed in γ-rays, hard X-rays, and sometimes at optical wavelengths. The afterglow is a long-lasting emission in X-rays, optical, and sometimes radio wavelengths following the prompt emission.

GRB light curves (LCs) observed by the Neil Gehrels Swift Observatory (Swift) have more complex features than a simple power-law (PL) decay (Sakamoto et al. 2007; Zhang et al. 2009). Sakamoto et al. (2007) discovered the existence of a flat part in the X-ray LCs of GRBs, the "plateau," which is present soon after the decaying phase of the prompt emission. The Swift plateaus generally last from hundreds to a few thousands of seconds (Willingale et al. 2007, hereafter W07), and are followed by a PL decay phase. Several models have been proposed to explain the plateau, one being the long-lasting energy injection from the central engine by fallback mass accretion onto a BH. This energy injection will be released into the external shock, where a single relativistic blast wave interacts with the surrounding medium (Zhang & Mészáros 2001; Liang et al. 2007; Oates et al. 2012). Another possibility is that the energy injection is produced by the spin-down luminosity of a millisecond newborn NS, the so-called magnetar (e.g., Rowlinson et al. 2014; Rea et al. 2015; Stratta et al. 2018; Fraija et al. 2020). In the investigation of the physical mechanisms that drive GRBs, the plateau found at

[15] T_{90} is the time over which a burst emits from 5% to 95% of its total measured counts in the prompt emission.

X-ray and optical wavelengths has been highlighted as a feature that could standardize the varied GRB population. Dainotti et al. (2016, 2017a, 2017b) and Li et al. (2018b) explored the relation between the luminosity L_a and rest-frame time T_a^* both measured at the end of the plateau (known as the Dainotti relation). We denote the rest-frame time with an asterisk. Rowlinson et al. (2014) showed that the Dainotti relation in X-rays can be naturally recovered within the magnetar scenario with a slope of -1. Within the cosmological context this correlation has already been applied to construct a GRB Hubble diagram out to $z > 8$ (Cardone et al. 2009, 2010; Postnikov et al. 2014; Dainotti et al. 2013). We investigate this correlation at optical wavelengths to determine how common the plateau is in optical LCs, and how tight the Dainotti relation is for a large optical sample. This work investigates if a similar correlation in the optical can be determined and can be applied as a reliable cosmological tool in the future.

As determined in Dainotti et al. (2016, 2017a, 2017b), it is necessary to select a subsample of GRBs with very well-defined characteristics from a morphological and/or a physical point of view to obtain a GRB class that can be standardized, because the tightness of the correlations may also depend on how the sample is divided into classes. The long/short classification has been challenged over the years with the discovery of several subclasses that may arise from different progenitors or the same progenitors with different surroundings. Such categories are: SGRBs with extended emission (SEE; Norris & Bonnell 2006; Levan et al. 2007; Norris et al. 2010) with mixed features between SGRBs and LGRBs; intrinsically short (IS) GRBs, with $T_{90}^* = T_{90}/(1+z) < 2$ s; X-ray flashes (XRFs) with unusually soft spectra and greater fluences in the X-ray band (2–30 keV) than in the gamma-ray band (30–400 keV; Heise et al. 2001); X-ray rich GRBs (XRRs) that are intermediate in spectral hardness between XRFs and usual GRBs (Liu & Mao 2019); ultralong GRBs (ULGRBs) with a very long prompt duration ($T_{90} > 1000$ s; Gendre et al. 2019); and GRBs associated with supernovae (GRB-SNe; Cano et al. 2017). Moreover, there are LGRBs for which an associated SN was not detected, but should have been detected given the observational limits. Examples are the nearby SN-less GRB 060505 and GRB 060614 (Kann et al. 2011; Ofek et al. 2007); these cases highlight the possibility of LGRBs with and without SNe. The categories of GRB-SNe are (A) strong spectroscopic evidence for an SN associated with the GRB; (B) a clear LC bump as well as some spectroscopic evidence suggesting the long GRB-SNe association; (C) a clear bump in the LC consistent with the GRB-SNe associations, but no spectroscopic evidence of the SN; (D) a significant bump in the LC, but the properties of the SN are not completely consistent with other GRB-SNe associations, or the bump is not well sampled, or there is lack of a spectroscopic redshift of the GRB; (E) a bump, with low significance or inconsistent with other GRB-SNe identifications, but with the presence of a GRB spectroscopic redshift (Hjorth & Bloom 2012).

A different classification based on physical mechanisms related to the GRBs' progenitors has been proposed (Zhang et al. 2009; Kann et al. 2011; Li et al. 2020), according to which GRBs are divided into Type I, powered by compact object mergers: the merger of two NSs or an NS and a BH, and in Type II, characterized by the collapse of massive stars. Type I GRBs include SGRBs, SEE, and IS, while Type II include the LGRBs, GRB-SNe, and XRFs. A diagram clarifying this classification is shown in Figure 8 of Zhang et al. (2009). To homogenize the morphological classification with the one that may arise from different progenitors or the same progenitors with different environments, we ascribe the GRB types in our sample to the Type I or Type II categories.

In Section 2 we detail our sample and data analysis, in Section 3 the methodology, and in Section 4 the results of the $L_{\rm opt} - T_{\rm opt}^*$ correlation. In Section 5 we summarize our conclusions.

2. Data Analysis and Sample Selection

We built a comprehensive sample of optical GRB LCs with known redshifts by searching the literature for all GRBs detected between 1997 May and 2019 January by several satellites such as the Swift Ultraviolet/Optical Telescope (UVOT), or ground-based telescopes/detectors (e.g., GROND). In our final sample the redshifts of the GRBs span from $z = 0.06$ to $z = 8.23$ and the LCs employed are found in Kann et al. (2006, 2010, 2011, 2021a, 2021b, in preparation), Li et al. (2012, 2015, 2018a), Oates et al. (2009, 2012), Zaninoni et al. (2013), and Si et al. (2018). We then determine the existence of a plateau by fitting the LCs with the phenomenological[16] W07 model; see Section 3.

Below, we summarize the data analysis used by Li et al. (2012, 2015, 2018a), Kann et al. (2006, 2010, 2011), Oates et al. (2012), Zaninoni et al. (2013), and Si et al. (2018). For GRBs that overlap between these samples, we choose the ones with the greatest coverage, especially in the plateau, and where the χ^2 value for the W07 fitting is the smallest. In some cases, more coverage introduces more scatter that reduces the quality of the fit; in these cases, we select the individual LCs rather than the combined LCs. We include five combined LCs in our final sample.

We use 10 GRBs from Li et al. (2012, 2015, 2018a, 2020) that meet our requirements defined in Section 3. Following Li et al. (2012, 2015, 2018a), we correct for Galactic extinction for the optical and NIR magnitudes, and for host-galaxy extinction correction through an extinction parameter $A_{\rm v}$, assuming $R_{\rm v} = 3.1$. The flux contribution coming from the host galaxy at very late times ($\sim 10^6$ s after the GRB trigger) for some GRBs has also been subtracted. For the GRBs that were not already corrected for host extinction in the papers cited previously, we computed the extinction factor as $-2.5 * \mathrm{Log}(A_{\rm v})$ in flux density space.

We use 57 LCs from Kann et al. (2006, 2010, 2011, 2021a, 2021b, in preparation). Following Kann et al. (2006), for each afterglow, the multiband LCs are fit with, depending on the detected features, a single PL, a smoothly broken PL, or a series of these. Additionally, if necessary, a constant host-galaxy component is added, and a special supernova-model fit is applied if such an SN is detected following the GRB (see Kann et al. 2019 for a specific example). The afterglow itself is assumed to evolve achromatically, and therefore the parameters of the afterglow evolution (decay slopes, break time, and smoothness) are shared among all bands (host-galaxy and SN parameters are individual to each band). These fits result in a spectral energy distribution (SED) that is determined by the entirety of the data; the SED is assumed to be constant. The SED is then used twofold: first, it allows (after necessary host- and SN-component removal) to shift other bands to the $R_{\rm C}$

[16] The W07 model makes no assumptions on the underlying physics.

band, for which there are essentially always measurements, creating a compound LC with maximized data density and temporal coverage. Furthermore, the SED can be analyzed to determine the line-of-sight extinction in the host galaxy. Then, the LCs are corrected for host-galaxy extinction.

From Oates et al. (2012) we use three GRBs that were constructed from multifilter LCs, following Oates et al. (2009). The main steps performed are to normalize the multifilter LCs to the v filter and then to group them using a bin size of $\Delta t/t = 0.2$. The LCs are then normalized to the R_C filter relative to the LCs from the Kann et al. (2006, 2010, 2011) sample that overlaps with the Oates et al. (2012) sample. In Oates et al. (2009), for each GRB, the onset of the prompt γ-ray emission (the start time of the T_{90} parameter) is equal to the start time of the UVOT LC. However, here we convert it using the Burst Alert Telescope (BAT) trigger time as the start time of the UVOT LCs to have a consistent BAT trigger time, as the other LCs in the sample. To correct for host extinction, for these three GRBs we use the same values as Oates et al. (2012).

We use 19 GRBs from Zaninoni et al. (2013). In this Letter, optical data are gathered from the literature and from various telescopes, and all units are converted from magnitudes to flux densities; the data are not initially corrected for reddening. SEDs are created at early and late times for each GRB, only using optical filters for which data were available; spectral index values $\beta_{\rm opt}$ are derived from fitting these SEDs, corrected for host and Galactic extinction.

We use 16 LCs investigated in Si et al. (2018). Their data come from Li et al. (2012) and Kann et al. (2006). We corrected this data for host extinction following Kann et al. (2006).

3. Methodology

Since the LCs are from different sources in different units, we converted all fluxes into erg cm^{-2} s^{-1} in the R band. We fit the W07 model in the observer frame. Its functional form is

$$f_i(t) = \begin{cases} F_i \exp\left(\alpha_i\left(1 - \frac{t}{T_i}\right)\right)\exp\left(-\frac{t_i}{t}\right) & \text{for } t < T_i \\ F_i\left(\frac{t}{T_i}\right)^{-\alpha_i}\exp\left(-\frac{t_i}{t}\right) & \text{for } t \geqslant T_i. \end{cases} \quad (1)$$

This function $f(t) = f_a(t) + f_p(t)$ is the sum of the two functions that represent both the prompt, f_p, and the afterglow emission, f_a. We focus on the afterglow. $f(t)$ contains sets of four free parameters (T_a, F_a, α_a, t_a) for each of the two functions f_a and f_p, where T_a is the time end of the plateau, F_a is its associated flux, α_a is the temporal PL decay index after the plateau, and the time t_a is the initial rise timescale of the afterglow. In the majority of cases t_a is compatible with zero, thus it is set as a fixed parameter. The time T_t is the time where $f_p(T_t) = f_a(T_t)$. Its associated flux is F_t. We do not fit the LCs with fewer than five data points because this would be too few compared to the fit parameters. Then, we exclude the cases when the fitting procedure fails or the determination of 1σ confidence intervals does not fulfill the χ^2 rules; see the XSPEC manual.[17] Out of the 267 GRBs analyzed, 102 LCs with well-defined plateaus constitute our final sample, composed of 35 LGRBs, 9 SGRBs (Jensen et al. 2001; Norris & Bonnell 2006; Levan et al. 2007; Norris et al. 2010; Zhang et al. 2009; Kaneko et al. 2015), 1 SGRB associated with a kilonova (Rossi et al. 2020), 12 XRFs (Bi et al. 2018; Levan et al. 2007; Ruffini et al. 2016), 44 XRRs (Bi et al. 2018), 23 GRB-SNe (Hjorth & Bloom 2012; Cano et al. 2017; Klose et al. 2019), and 4 ULGRBs (Gruber et al. 2011; Gendre et al. 2019). Some GRBs are repeated because they can belong to multiple classes. See Figure 1 for two examples of well-defined plateaus in our sample. We reject 59 LCs for PL behavior, 52 for having too few points or being too scattered, and 54 for having $\Delta\chi^2$ not fulfilling the χ^2 prescriptions.

Once we fitted the LCs, we compute from the the optical observed flux $F_{\rm opt}$ (erg cm^{-2} s^{-1}) the optical luminosity in the R_C filter (one GRB is in the V band and another is in H band), $L_{\rm opt}$ (in units of erg s^{-1}), using the following:

$$L_{\rm opt} = 4\pi D_L^2(z)\, F_{\rm opt}(T_{\rm opt}) \cdot K \quad (2)$$

at the time $T^*_{\rm opt}$ at the end of the optical plateau, where $D_L(z)$ is the luminosity distance, assuming a flat Λ cold dark matter (ΛCDM) cosmological model with $\Omega_M = 0.3$ and $H_0 = 70\,{\rm km\,s^{-1}}$ Mpc^{-1}. The k-correction K (Bloom et al. 2001) is

$$K = \frac{1}{(1+z)^{1-\beta_{\rm opt}}}, \quad (3)$$

where $\beta_{\rm opt}$ is the optical spectral index of the GRB. The optical spectral parameters are gathered from the literature; for GRBs where $\beta_{\rm opt}$ is unknown, we average values of the whole sample and we use the mean square error (MSE) as the error: $\beta_{\rm opt} = 0.79 \pm 0.03$.

The Gold sample is a subsample of GRB LCs with at least four points at the start time of the plateau emission and with plateau inclination $\leqslant 41^\circ$ (for details, see Dainotti et al. 2016). The inclination is defined using trigonometry as $\frac{\Delta F}{\Delta t} = \frac{F_t - F_a}{T_a - T_t}$. These criteria ensure the plateau is well defined and shallow enough not to be considered a simple PL. The Gold sample consists of seven GRBs.

4. The Luminosity–Time Correlation for Optical Plateaus

Following Dainotti et al. (2017b) we investigate the PL relation between the optical luminosity and rest-frame time at the end of the optical plateau: the $L_{\rm opt}$–$T^*_{\rm opt}$ correlation for 102 GRBs; see Figure 1. The best-fit parameters are calculated using the linear least-squares method with the command LinearModelFit in Mathematica 12.1 using the variables in the log scale for convenience. LinearModelFit constructs a linear model of the form $< y > = \gamma_0 + \gamma_1\, x_1 + \gamma_2\, x_2 + \ldots$ that fits the y_i for successive x values 1, 2... under the assumption that the original y_i are independent normally distributed. In our case $y_i = \log L_{i,\rm opt}$ and $x_i = \log T^*_{i,\rm opt}$, where i denotes the GRBs in the sample. In this Letter uncertainties are quoted at 1σ, and we do not account for selection biases and redshift evolution as discussed in Dainotti et al. (2013, 2017a). We will address this problem in a forthcoming paper. Here we investigate whether the luminosity–time correlation holds for a large sample of optical plateaus, if there are classes favored because they have small squared scatter, hereafter σ^2, and the similarities and differences between the luminosity–time correlation in X-rays and in optical.

[17] https://heasarc.gsfc.nasa.gov/xanadu/xspec/manual/node10.html

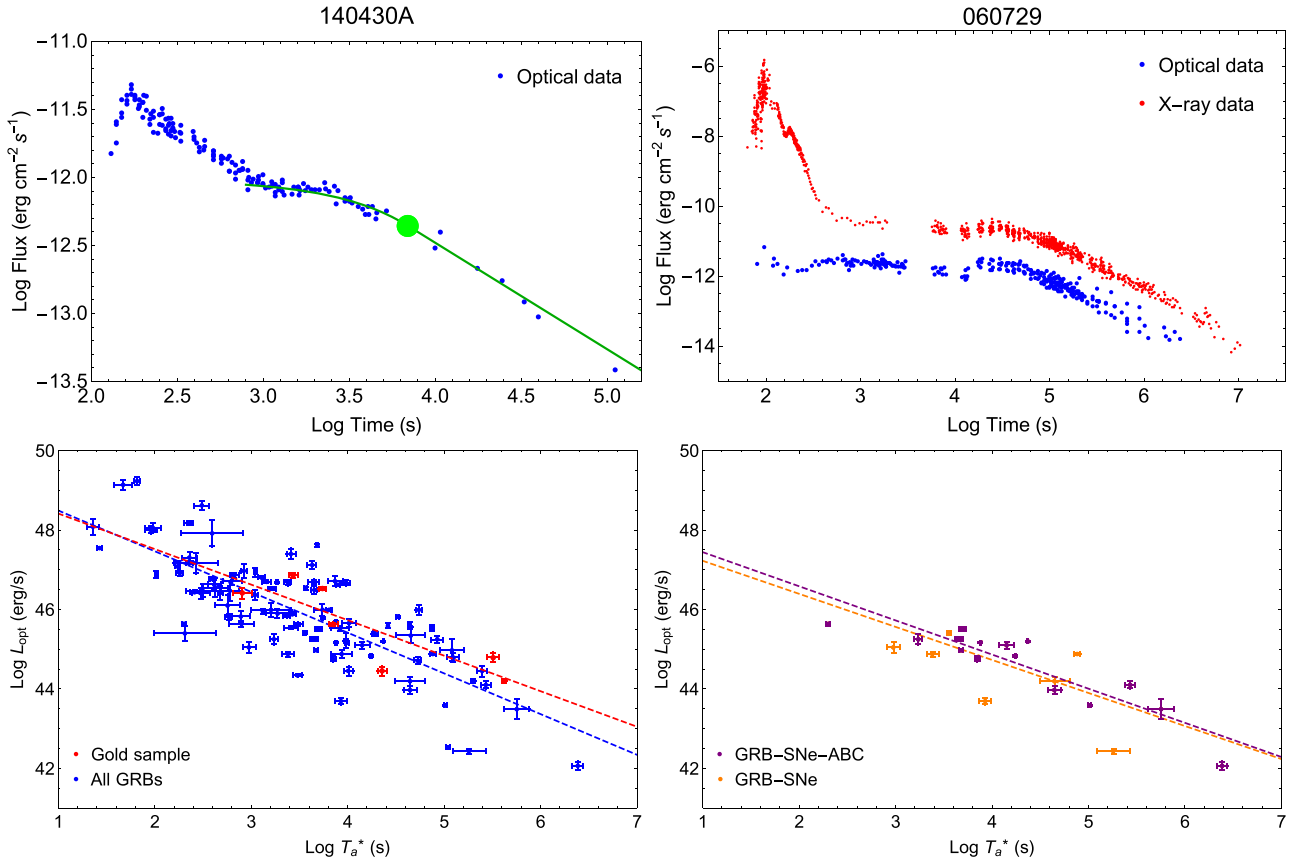

Figure 1. Upper left: the W07 fit for a well-sampled optical plateau shown as a green line, with the green dot representing ($T^*_{\rm opt}$, $L_{\rm opt}$). Optical data are from D. A. Kann et al. (2021a, in preparation). The fits were performed with error bars, which are not shown so as not to clutter the graph. Upper right: another example of a well-sampled LC with the coincident observation of the X-ray plateau. The optical LC is from Zaninoni et al. (2013), while the X-ray LC is from the Swift X-ray Telescope (XRT) repository. Lower panels: the $L_{\rm opt}$–$T^*_{\rm opt}$ relation for the Gold and the total sample (left) and for the GRB-SNe total and the GRB-SNe (A,B,C) (right). The best-fit lines are calculated using a linear model fit in log scale and plotted in matching colors as dashed lines.

Table 1
The Best-Fit Parameters for Various Subsamples

Class	a_{opt}	C_o	N	ρ	P	$\lvert\Delta\rho\rvert$	σ^2 of the fit	$\delta\sigma^2$
All GRBs	-1.02 ± 0.16	49.52 ± 0.58	102	-0.77	2.7×10^{-23}	0	0.63	0.0%
Gold	-0.89 ± 0.64	49.31 ± 2.75	7	-0.86	1.6×10^{-2}	10.5%	0.30	−52.4%
SGRBs	-1.11 ± 1.06	49.73 ± 4.34	9	-0.80	4.4×10^{-2}	3.75%	0.49	−22.2%
LGRBs	-0.86 ± 0.26	49.25 ± 0.91	35	-0.75	1.1×10^{-7}	2.7%	0.86	+36.0%
XRFs	-0.97 ± 0.43	48.53 ± 1.81	12	-0.82	5.7×10^{-4}	6.09%	0.76	+20.6%
GRB-XRR	-1.14 ± 0.24	49.89 ± 0.84	44	-0.80	4.0×10^{-12}	3.8%	0.81	+28.6%
GRB-SNe	-0.83 ± 0.27	48.06 ± 1.16	23	-0.77	2.3×10^{-6}	0%	1.00	+58.7%
GRB-SNe-ABC	-0.86 ± 0.24	48.30 ± 1.04	16	-0.85	2.0×10^{-6}	9.4%	0.79	+25.4%

Note. The variance is the population variance, defined as $\sigma^2 = \frac{\sum(X-\mu^2)}{N}$ for a given subsample of N GRBs.
The best-fit parameters for each subsample are calculated using a linear model fit in log scale in mathematica 12.1: $a_{\rm opt}$ is the slope of the correlation, C_0 is the normalization constant, N is the number of GRBs in each subsample, ρ is the Spearman correlation coefficient, P is the probability that these correlations occur by chance, and $|\Delta\rho|$ is the absolute value of the change in percentage in the ρ of each class relative to all GRBs.

The optical luminosity–time relation is defined as

$$\log L_{\rm opt} = C_o + a_{\rm opt} \times \log T^*_{\rm opt}, \quad (4)$$

where $C_{\rm o}$ is the normalization constant, and $a_{\rm opt}$ is the best-fit parameter representing the slope of the correlation in optical. To make the units dimensionless $T^*_{\rm opt}$ is divided by 1 s. The best-fit parameters of the total sample, and other subsamples along with their squared scatter, are shown in Table 1. There are only four ULGRBs, so they are not included in Table 1. We also present in Table 2 the identity of the GRB, ID GRB, the redshift, T_{90}, the fitted parameters of the W07 model, the spectral index $\beta_{\rm opt}$, and $\log L_{\rm opt}$ of the plateau phase.

Table 2
Best-Fit Parameters for Willingale Model

ID GRB	z	T_{90}	Class	$\log F_{\rm opt}$	$\log T_{\rm op}$	$\alpha_{\rm opt}$	$\beta_{\rm opt}$	$\log L_{\rm opt}$	Data Source
000301C	2.03	2.00	IS	-13.83 ± 0.12	5.88 ± 0.05	2.85 ± 0.14	0.59 ± 0.12	44.45 ± 0.14	Si18
000926	2.04	25.00	L	-12.89 ± 0.03	5.12 ± 0.02	2.14 ± 0.04	1.01 ± 0.16	45.60 ± 0.08	Kann06
011211	2.14	270.00	L	-13.52 ± 0.06	5.23 ± 0.04	1.98 ± 0.11	0.41 ± 0.14	44.72 ± 0.09	Kann10
021004	2.34	100.00	L	-12.92 ± 0.02	5.40 ± 0.02	1.33 ± 0.03	0.67 ± 0.14	45.53 ± 0.08	Li12, Li15
030226	1.99	22.09	L	-12.44 ± 0.04	3.24 ± 0.04	1.33 ± 0.05	0.57 ± 0.12	45.81 ± 0.07	Kann06
030328	1.52	199.20	L	-12.70 ± 0.02	4.38 ± 0.02	1.25 ± 0.04	0.36 ± 0.45	45.22 ± 0.18	Kann06
030329	0.17	62.90	SN-A	-11.76 ± 0.09	5.50 ± 0.05	1.46 ± 0.03	0.41 ± 0.17	44.11 ± 0.09	Si18
040924	0.86	2.39	SN-C	-12.20 ± 0.04	3.50 ± 0.04	1.30 ± 0.02	0.63 ± 0.48	45.26 ± 0.13	Kann06
041006	0.72	17.40	SN-C	-12.45 ± 0.03	4.08 ± 0.03	1.24 ± 0.01	0.36 ± 0.27	44.76 ± 0.07	Si18
050319	3.24	152.54	XRR	-12.83 ± 0.02	4.44 ± 0.03	0.76 ± 0.03	0.76 ± 0.02	45.99 ± 0.02	Zaninoni13
050408	1.24	34.00	L	-13.25 ± 0.03	4.36 ± 0.05	0.83 ± 0.05	0.28 ± 0.33	44.45 ± 0.12	Si18
050416A	0.65	2.49	XRF-D-IS-SN	-13.54 ± 0.05	4.15 ± 0.06	0.94 ± 0.08	0.92 ± 0.30	43.70 ± 0.08	Li12, Li15
050502A	3.79	20.00	L	-12.60 ± 0.04	3.72 ± 0.03	1.43 ± 0.02	0.76 ± 0.16	46.36 ± 0.11	Kann10
050525A	0.61	8.83	SN-B-XRR	-11.57 ± 0.04	3.90 ± 0.04	1.44 ± 0.03	0.52 ± 0.08	45.51 ± 0.04	Kann10
050603	2.82	21.00	L	-11.88 ± 0.13	4.45 ± 0.08	1.85 ± 0.09	0.60 ± 0.00	46.71 ± 0.13	Kann10
050730	3.97	156.50	L	-12.15 ± 0.04	4.34 ± 0.06	1.57 ± 0.07	0.52 ± 0.05	46.69 ± 0.05	Kann10
050801	1.56	19.40	XRR	-10.98 ± 0.02	2.64 ± 0.02	1.19 ± 0.01	0.69 ± 0.34	47.09 ± 0.14	Kann10
050802	1.71	30.00	L	-11.61 ± 0.08	2.91 ± 0.09	0.91 ± 0.01	0.36 ± 0.26	46.41 ± 0.14	Kann10
050820A	2.61	244.69	L	-11.97 ± 0.01	4.46 ± 0.02	1.02 ± 0.01	0.72 ± 0.03	46.62 ± 0.02	Kann10; Zaninoni13
050824	0.83	22.58	XRF-E-SN	-12.50 ± 0.03	3.65 ± 0.06	0.65 ± 0.01	0.45 ± 0.18	44.87 ± 0.06	Kann10
050908	3.34	17.37	XRR	-12.61 ± 0.08	3.26 ± 0.13	0.82 ± 0.08	1.25 ± 0.36	46.55 ± 0.24	Zaninoni13
050922C	2.20	4.54	IS	-11.65 ± 0.01	3.77 ± 0.01	1.25 ± 0.01	0.56 ± 0.01	46.69 ± 0.01	Kann10; Zaninoni13; Oates09, Oates12
051109A	2.35	37.23	L	-12.14 ± 0.03	3.74 ± 0.04	0.81 ± 0.02	1.06 ± 0.06	46.52 ± 0.04	Zaninoni13
051111	1.55	59.78	L	-10.91 ± 0.03	2.77 ± 0.04	1.00 ± 0.04	0.76 ± 0.07	47.18 ± 0.04	Si18
060124	2.30	13.63	XRR	-11.66 ± 0.03	3.63 ± 0.04	0.88 ± 0.00	0.75 ± 0.01	46.81 ± 0.03	Zaninoni13
060206	4.05	7.59	XRR-IS	-12.05 ± 0.01	4.39 ± 0.01	1.39 ± 0.01	1.66 ± 0.05	47.62 ± 0.04	Zaninoni13
060210	3.91	255.00	L	-11.70 ± 0.14	3.05 ± 0.08	1.49 ± 0.05	0.76 ± 0.00	47.30 ± 0.14	Kann10
060418	1.49	144.00	XRR	-10.01 ± 0.09	2.35 ± 0.06	1.23 ± 0.01	0.69 ± 0.11	48.01 ± 0.10	Kann10
060512	0.44	8.49	XRF	-12.44 ± 0.03	3.64 ± 0.05	0.74 ± 0.02	0.60 ± 0.00	44.35 ± 0.03	Kann10
060526	3.21	298.16	XRR	-12.20 ± 0.01	4.19 ± 0.01	1.12 ± 0.01	0.65 ± 0.06	46.54 ± 0.04	Kann10
060605	3.78	114.79	XRR	-11.16 ± 0.04	3.03 ± 0.05	1.04 ± 0.04	1.32 ± 0.03	48.18 ± 0.05	Zaninoni13
060607A	3.07	99.30	L	-11.78 ± 0.03	3.53 ± 0.04	1.25 ± 0.05	0.72 ± 0.27	46.97 ± 0.17	Kann10
060614	0.13	108.70	KN-SEE-XRR	-13.05 ± 0.04	5.09 ± 0.02	2.15 ± 0.02	0.47 ± 0.04	42.53 ± 0.04	Si18; Zaninoni13
060714	2.71	114.99	XRR	-12.47 ± 0.17	3.77 ± 0.21	0.76 ± 0.07	0.44 ± 0.04	45.99 ± 0.18	Si18
060729	0.54	115.35	XRR-SN-E	-12.15 ± 0.03	5.07 ± 0.03	1.26 ± 0.06	0.85 ± 0.01	44.88 ± 0.03	Zaninoni13
060904B	0.70	171.47	XRR-SN-C	-12.11 ± 0.04	3.89 ± 0.04	1.20 ± 0.03	1.11 ± 0.10	45.25 ± 0.05	Kann10
060927	5.46	22.54	XRR	-12.19 ± 0.26	3.24 ± 0.23	1.26 ± 0.06	0.82 ± 0.00	47.17 ± 0.26	Kann10
061007	1.26	75.31	L	-8.76 ± 0.07	2.17 ± 0.03	1.75 ± 0.01	1.07 ± 0.19	49.23 ± 0.09	Kann10
061121	1.31	81.25	L	-12.27 ± 0.04	3.85 ± 0.05	1.00 ± 0.01	0.68 ± 0.06	45.62 ± 0.05	Zaninoni13
070110	2.35	88.42	XRR	-12.90 ± 0.06	4.44 ± 0.10	0.99 ± 0.05	0.60 ± 0.00	45.52 ± 0.06	Kann10
070125	1.55	60.00	L	-12.25 ± 0.13	5.14 ± 0.03	2.37 ± 0.08	1.13 ± 0.02	45.99 ± 0.13	Zaninoni13
070208	1.17	64.00	XRR	-12.37 ± 0.19	2.65 ± 0.32	0.52 ± 0.03	0.66 ± 0.00	45.40 ± 0.19	Kann10
070411	2.95	122.75	XRR	-12.50 ± 0.19	3.38 ± 0.10	2.01 ± 0.31	1.17 ± 0.27	46.47 ± 0.25	Zaninoni13
070419A	0.97	160.00	XRF-SN-D	-12.67 ± 0.12	3.27 ± 0.07	1.40 ± 0.05	1.11 ± 0.22	45.05 ± 0.14	Zaninoni13
070810A	2.17	11.03	XRR	-12.45 ± 0.11	3.77 ± 0.12	1.50 ± 0.11	0.60 ± 0.00	45.90 ± 0.11	Kann10
071003	1.60	148.13	L	-13.16 ± 0.07	5.51 ± 0.06	2.17 ± 0.15	0.35 ± 0.23	44.79 ± 0.12	Kann10
071010A	0.99	6.20	L	-11.12 ± 0.16	2.80 ± 0.17	0.81 ± 0.02	0.61 ± 0.12	46.47 ± 0.16	Kann10
071025	5.00	238.14	XRR	-12.58 ± 0.03	3.37 ± 0.02	1.41 ± 0.01	0.93 ± 0.03	46.78 ± 0.03	Kann10
071031	2.69	180.89	XRF	-11.99 ± 0.03	3.25 ± 0.03	0.85 ± 0.01	0.34 ± 0.30	46.41 ± 0.17	Kann10
071112C	0.82	15.00	SN-C	-11.73 ± 0.01	2.56 ± 0.02	0.92 ± 0.00	0.44 ± 0.11	45.64 ± 0.03	D. A. Kann (2021b, in preparation)

Note. The data source codes are first author followed by publication year: for example, Si2018 corresponds to Si et al. (2018). Combined LCs have multiple authors listed. The full table with 102 GRBs is available at http://www.oa.uj.edu.pl/M.Dainotti/GRB2020/.
Includes the Identity of the GRB, ID GRB, its redshift, z, T_{90}, and the best-fit parameters calculated using the W07 model: the optical flux at the end of the plateau, $\log F_{\rm opt}$, the end time of the plateau $\log T_{\rm opt}$, the slope after the plateau, $\alpha_{\rm opt}$, the optical spectral index, $\beta_{\rm opt}$, and the optical luminosity at the end of the plateau, $L_{\rm opt}$.

For the total sample, the resulting luminosity–time relation follows the form of Equation (4) with constants: $C_{\rm o} = 49.52 \pm 0.58$, $a_{\rm opt} = -1.02 \pm 0.16$, and $\sigma^2 = 0.63$. The Spearman correlation coefficient, $\rho = -0.77$, and the probability of this correlation occurring by chance, P, is 2.7×10^{-23}. For all classes ρ is very high and $P \ll 0.05$. This behavior is consistent across all classes, thus guaranteeing that this correlation holds regardless of class. The luminosity–time

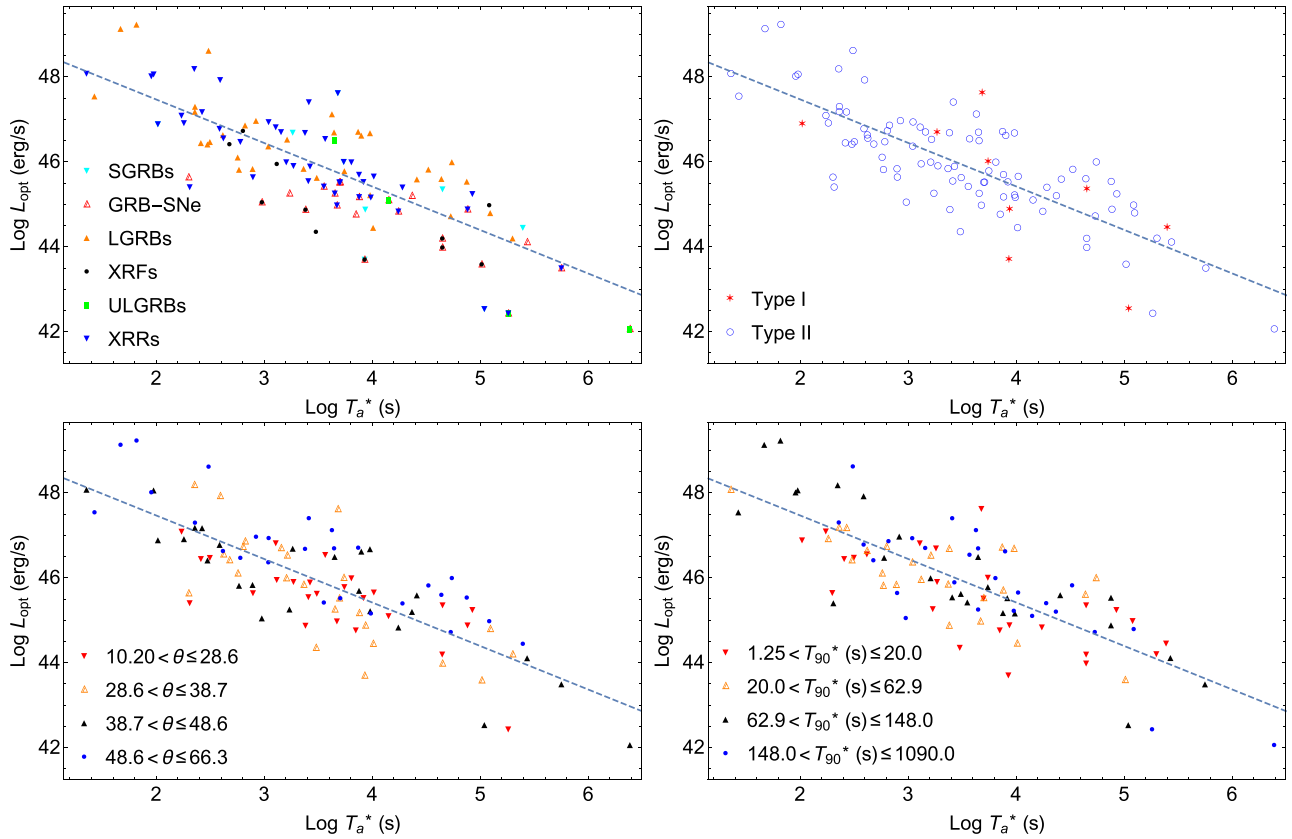

Figure 2. The L_{opt}–T^*_{opt} relation, plotted according to class, type (I or II), plateau angle, and T^*_{90}. The best-fit lines shown here represent the slope of the total sample of 102 GRBs, calculated using the a linear model fit in log scale in Mathematica 12.1, and are plotted as dashed lines.

correlation holds in optical afterglows even for this sample of 102 GRBs, which is the largest compilation of optical plateaus so far in the literature. The slopes of the luminosity–time correlation in X-ray and optical for a common overlapping sample agree within 1σ, $_{aX} = -1.32 \pm 0.28$ and $a_{opt} = -1.12 \pm 0.26$; thus, we can infer that the energy reservoir of the GRB during the plateau in both electromagnetic regimes is constant and is independent of class (the best-fit slopes through each of the classes are $a \approx -1$; see Table 1).

The Gold sample has a $\sigma^2 = 0.30$, smaller than that of the total sample by 52.4%. To compare the tightness of the correlation in optical and in X-rays, we identify the GRBs coincident between our optical sample and the X-ray sample of Srinivasaragavan et al. (2020) and Dainotti et al. (2020); the two samples have 56 GRBs in common. From the fit of these 56 GRBs we obtain the following X-ray and optical parameters: $C_{0,X} = 52.02 \pm 0.99$, $_{aX} = 1.32 \pm 0.28$, while $C_{0,opt} = 49.91 \pm 0.91$, $a_{opt} = 1.12 \pm 0.26$. This leads us to conclude that the luminosity–time correlation in X-rays is tighter than in optical. Since in both cases within errors the slope of the correlation is compatible with -1, this implies that the energy reservoir of the plateau is constant and that a magnetar scenario can be the leading explanation for the optical correlation as well as for the X-ray one.

The first panel of Figure 2 shows our sample divided by class. No class clusters in a particular region of the plot. Indeed, both the slope a_{opt} and the normalization agree within 1σ for all classes; ρ for all classes are shown in Table 1. The gold class has the highest correlation coefficient and the smallest squared scatter, $\sigma^2 = 0.30$, with a percentage decrease compared to all GRBs of 52.4%; see the last column of Table 1. This is aligned with a previous result shown in Dainotti & Del Vecchio (2017) and Dainotti et al. (2016): the Gold sample has a much higher correlation coefficient, and a smaller scatter also in X-rays.

The second panel of Figure 2 shows the distinction between Type I and Type II GRBs.

The third panel of Figure 2 represents all GRBs binned by the angle of inclination of the plateau feature. For each of the angle bins in increasing order $\rho = (-0.65, -0.78, -0.86, -0.83)$, where the third bin ($38.^\circ7 < \theta \leqslant 48.^\circ6$, black triangles in figure) shows the tightest correlation.

The fourth panel of Figure 2 shows all GRBs divided by T^*_{90}; ρ for each of the T^*_{90} bins, in increasing order, are $\rho = (-0.73, -0.66, -0.85, -0.75)$. The third bin ($62.9s < T^*_{90} < 148.0s$) has the highest monotonic correlation.

5. Discussion and Conclusions

We have gathered the largest compilation of optical plateaus to date (102 GRBs) and shown that the L_{opt}–T^*_{opt} correlation holds for a sample that is more than double the largest sample presented in the literature. The optical correlation is

$$\log L_{opt} = (49.52 \pm 0.58) - (1.02 \pm 0.16) \times \log T^*_{opt}, \quad (5)$$

with $\sigma^2 = 0.63$ and $\rho = -0.77$ for the whole sample. The Gold sample has a reduced $\sigma^2 = 0.30$ of 52.4% and an increased $\rho = -0.86$ (10.5% increase; see Table 1 for the absolute value of Δ_ρ). The slopes of the X-ray and optical luminosity–time correlation are within 1σ; both demonstrate strong linear anticorrelations. Given the slope of the correlation is nearly -1, this further supports that the plateau has a fixed

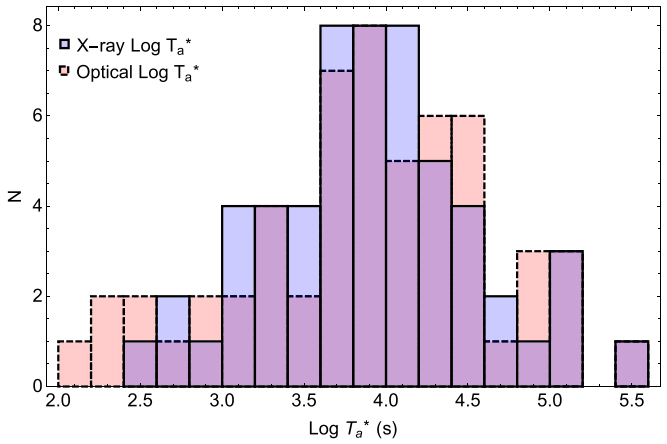

Figure 3. The differential histogram of the end time of the plateau in the rest frame for the optical (in red) and X-ray (in blue) afterglow. The violet colors are the ones coincident between X-rays and optical.

energy reservoir independent of a given class and a possible explanation can be the magnetar model. The source of the scatter of the correlation comes both from a physical point of view, depending on the energy mechanism underlying the plateau, which regime and frequency, and from an instrumental point of view. We indeed obtain a reduced scatter when we consider LCs belonging to the Gold sample. Additionally, we find that the $L_{\rm opt}$–$T^*_{\rm opt}$ correlation holds regardless of GRB class, plateau angle, or T^*_{90}.

Furthermore, we find that the end time of the plateau is achromatic between X-ray and optical observations for a subsample of GRBs observed in both bands (see Figure 3). It is compelling that the candidate feature, the plateau, to standardize GRBs is achromatic between the X-rays and optical, the two wavelengths in which the majority of plateaus are observed. This analysis can be ascribed to a larger context for the determination of whether or not the plateau is achromatic, since some cases of plateaus have been also observed by the Fermi-LAT in high-energy gamma-rays (Ajello et al. 2019).

This work made use of data supplied by the UK Swift Science Data Centre at the University of Leicester. We thank G. Sarracino for his help in modifying our host extinction code in Python, R. Wagner for the fitting of some GRB LCs, L. and A. Zambrano Tapia, M. Fuentes Quiñonez, and E. Fernández Guzmánn for the help in bibliography and combining some LCs. M.G.D acknowledges the American Astronomical Society Chretienne Grant for its initial support. D.A.K. acknowledges support from Spanish National Research Project RTI2018-098104-J-I00 (GRBPhot). We thank E. Cuellar for his guidance and his work in organizing the SULI summer program. This work was supported in part by the U.S. Department of Energy, Office of Science, Office of Workforce Development for Teachers and Scientists (WDTS) under the Science Undergraduate Laboratory Internships (SULI) program. Parts of this research were conducted by the Australian Research Council Centre of Excellence for Gravitational Wave Discovery (OzGrav), through project number CE170100004.

ORCID iDs

M. G. Dainotti https://orcid.org/0000-0003-4442-8546
S. Livermore https://orcid.org/0000-0002-7340-436X
D. A. Kann https://orcid.org/0000-0003-2902-3583
L. Li https://orcid.org/0000-0002-1343-3089
B. Zhang https://orcid.org/0000-0002-9725-2524
B. Gendre https://orcid.org/0000-0002-9077-2025
B. Cenko https://orcid.org/0000-0003-1673-970X
N. Fraija https://orcid.org/0000-0002-0173-6453

References

Abbott, B. P., Abbott, R., Abbott, T. D., et al. 2017, ApJL, 848, L12
Ajello, M., Arimoto, M., Axelsson, M., et al. 2019, ApJ, 878, 52
Bi, X., Mao, J., Liu, C., & Bai, J.-M. 2018, ApJ, 866, 97
Bloom, J. S., Frail, D. A., & Sari, R. 2001, AJ, 121, 2879
Cano, Z., Wang, S.-Q., Dai, Z.-G., & Wu, X.-F. 2017, AdAst, 2017, 8929054
Cardone, V. F., Capozziello, S., & Dainotti, M. G. 2009, MNRAS, 400, 775
Cardone, V. F., Dainotti, M. G., Capozziello, S., & Willingale, R. 2010, MNRAS, 408, 1181
Dainotti, M. G., Cardone, V. F., Piedipalumbo, E., & Capozziello, S. 2013, MNRAS, 436, 82
Dainotti, M. G., & Del Vecchio, R. 2017, NewAR, 77, 23
Dainotti, M. G., Hernandez, X., Postnikov, S., et al. 2017a, ApJ, 848, 88
Dainotti, M. G., Lenart, A., Sarracino, G., et al. 2020, arXiv:2010.02092
Dainotti, M. G., Nagataki, S., Maeda, K., Postnikov, S., & Pian, E. 2017b, A&A, 600, A98
Dainotti, M. G., Petrosian, V., Singal, J., & Ostrowski, M. 2013, ApJ, 774, 157
Dainotti, M. G., Postnikov, S., Hernandez, X., & Ostrowski, M. 2016, ApJL, 825, L20
Fraija, N., Betancourt Kamenetskaia, B., Dainotti, M. G., et al. 2020, arXiv:2006.04049
Gendre, B., Joyce, Q. T., Orange, N. B., et al. 2019, MNRAS, 486, 2471
Gruber, D., Krühler, T., Foley, S., et al. 2011, A&A, 528, A15
Heise, J., Zand, J. I., Kippen, R. M., & Woods, P. M. 2001, in Proc. ESO Astrophysics Symp., Gamma-ray Bursts in the Afterglow Era, ed. E. Costa, F. Frontera, & J. Hjorth (Berlin: Springer), 16
Hjorth, J., & Bloom, J. S. 2012, Gamma-ray Bursts (Cambridge: Cambridge Univ. Press)
Jensen, B. L., Fynbo, J. U., Gorosabel, J., et al. 2001, A&A, 370, 909
Kaneko, Y., Bostancı, Z. F., Göğüş, E., & Lin, L. 2015, MNRAS, 452, 824
Kann, D. A., Klose, S., & Zeh, A. 2006, ApJ, 641, 993
Kann, D. A., Klose, S., Zhang, B., et al. 2010, ApJ, 720, 1513
Kann, D. A., Klose, S., Zhang, B., et al. 2011, ApJ, 734, 96
Kann, D. A., Schady, P., Olivares, E. F., et al. 2019, A&A, 624, A143
Klose, S., Schmidl, S., Kann, D. A., et al. 2019, A&A, 622, A138
Kouveliotou, C., Meegan, C. A., Fishman, G. J., et al. 1993, ApJL, 413, L101
Levan, A. J., Jakobsson, P., Hurkett, C., et al. 2007, MNRAS, 378, 1439
Li, L., Liang, E.-W., Tang, Q.-W., et al. 2012, ApJ, 758, 27
Li, L., Wang, Y., Shao, L., et al. 2018a, ApJS, 234, 26
Li, L., Wu, X.-F., Huang, Y.-F., et al. 2015, ApJ, 805, 13
Li, L., Wu, X.-F., Lei, W.-H., et al. 2018b, ApJS, 236, 26
Li, Y., Zhang, B., & Yuan, Q. 2020, ApJ, 897, 154
Liang, E.-W., Zhang, B.-B., & Zhang, B. 2007, ApJ, 670, 565
Liu, C., & Mao, J. 2019, ApJ, 884, 59
Mazets, E. P., Golenetskii, S. V., Ilinskii, V. N., et al. 1981, Ap&SS, 80, 3
Norris, J. P., & Bonnell, J. T. 2006, ApJ, 643, 266
Norris, J. P., Gehrels, N., & Scargle, J. D. 2010, ApJ, 717, 411
Oates, S. R., Page, M. J., De Pasquale, M., et al. 2012, MNRAS, 426, L86
Oates, S. R., Page, M. J., Schady, P., et al. 2009, MNRAS, 395, 490
Ofek, E. O., Cenko, S. B., Gal-Yam, A., et al. 2007, ApJ, 662, 1129
Postnikov, S., Dainotti, M. G., Hernandez, X., & Capozziello, S. 2014, ApJ, 783, 126
Rea, N., Gullón, M., Pons, J. A., et al. 2015, ApJ, 813, 92
Riess, A. G., Rodney, S. A., Scolnic, D. M., et al. 2018, ApJ, 853, 126
Rossi, A., Stratta, G., Maiorano, E., et al. 2020, MNRAS, 493, 3379
Rowlinson, A., Gompertz, B. P., Dainotti, M., et al. 2014, MNRAS, 443, 1779
Ruffini, R., Rueda, J. A., Muccino, M., et al. 2016, ApJ, 832, 136
Sakamoto, T., Hill, J. E., Yamazaki, R., et al. 2007, ApJ, 669, 1115
Si, S.-K., Qi, Y.-Q., Xue, F.-X., et al. 2018, ApJ, 863, 50

Srinivasaragavan, G. P., Dainotti, M. G., Fraija, N., et al. 2020, arXiv:2009.06740
Stratta, G., Dainotti, M. G., Dall'Osso, S., Hernandez, X., & De Cesare, G. 2018, ApJ, 869, 155
Tanvir, N. R., Fox, D. B., Levan, A. J., et al. 2009, Natur, 461, 1254
Willingale, R., O'Brien, P. T., Osborne, J. P., et al. 2007, ApJ, 662, 1093
Woosley, S. E. 1993, ApJ, 405, 273
Zaninoni, E., Bernardini, M. G., Margutti, R., Oates, S., & Chincarini, G. 2013, A&A, 557, A12
Zhang, B., & Mészáros, P. 2001, ApJL, 552, L35
Zhang, B., Zhang, B.-B., Virgili, F. J., et al. 2009, ApJ, 703, 1696